

Tip Clearance Investigation of a Ducted Fan Used in VTOL Unmanned Aerial Vehicles—Part 1: Baseline Experiments and Computational Validation

Ali Akturk¹

e-mail: akturkali@gmail.com

Cengiz Camci²

Professor

e-mail: cxc11@psu.edu

Turbomachinery Aero-Heat Transfer Laboratory,
Department of Aerospace Engineering,
Pennsylvania State University,
University Park, PA 16802

Ducted fans that are popular choices in vertical take-off and landing (VTOL) unmanned aerial vehicles (UAV) offer a higher static thrust/power ratio for a given diameter than open propellers. Although ducted fans provide high performance in many VTOL applications, there are still unresolved problems associated with these systems. Fan rotor tip leakage flow is a significant source of aerodynamic loss for ducted fan VTOL UAVs and adversely affects the general aerodynamic performance of these vehicles. The present study utilized experimental and computational techniques in a 559 mm diameter ducted fan test system that has been custom designed and manufactured. The experimental investigation consisted of total pressure measurements using Kiel total pressure probes and real time six-component force and torque measurements. The computational technique used in this study included a 3D Reynolds-averaged Navier–Stokes (RANS) based computational fluid dynamics model of the ducted fan test system. Reynolds-averaged Navier–Stokes simulations of the flow around the rotor blades and duct geometry in the rotating frame of reference provided a comprehensive description of the tip leakage and passage flow. The experimental and computational analysis performed for various tip clearances were utilized in understanding the effect of the tip leakage flow on the aerodynamic performance of ducted fans used in VTOL UAVs. The aerodynamic measurements and results of the RANS simulations showed good agreement, especially near the tip region. [DOI: 10.1115/1.4023468]

1 Introduction

The flow field resulting from the region between the stationary duct and rotor tip of a ducted fan is complicated because of the interaction of the tip leakage flow, annulus wall boundary layer, and rotor wake. The inherent pressure difference between the pressure side and suction side of the blade tip generates a tip leakage flow. The leakage flow also rolls into a highly three dimensional tip leakage vortex with significantly turbulent and unsteady flow features in each passage. The tip leakage vortex is a complex flow phenomenon that is one of the dominant mechanisms of noise generation by unsteady interactions in a turbomachinery system. It is a significant energy loss mechanism in the ducted fans.

This paper describes investigations on the tip clearance flow for ducted fans. The common design principle of a ducted fan is to ensure that the tip clearance is as small as possible to reduce tip leakage losses and improve the aerodynamic performance. Indeed, this is still the case for ducted fans used in VTOL UAVs; the clearance is unavoidably kept large because of the operating conditions. There are many small diameter VTOL UAV systems using internal combustion (IC) engines as the power source. The IC engine driven systems suffer from strong mechanical vibrations.

There have been a limited number of studies about the three dimensional flow structure of leakage vortex in axial flow fans

and compressors in the literature [1–6]. Inoue and Kuroumaru et al. [7] made detailed flow measurements before and behind an axial flow rotor with different tip clearances. In their study, they investigated the clearance effect on the behavior of tip leakage flow. Furukawa and Inoue et al. [8] also investigated the breakdown of the tip leakage vortex in a low speed axial flow compressor. Reducing the tip leakage mass flow rate, in general, improves the aerodynamic performance of axial flow fans and compressors. Implementation of treatments in the nonrotating part over the blade tip is also an efficient method for tip leakage flow reduction. References [9,10] investigate different casing treatments for axial flow compressors.

The wake developed from an axial flow fan has a strong influence on the system performance. It is a significant source of aerodynamic loss and affects the efficiency and vibration characteristics. References [11–13] deal with extensive investigations of the wake flow features such as the mean velocities, turbulence, and decay characteristics on turbomachinery performance. The wake flow system is likely to interact with the complex flow system originating in the tip gap region.

Few authors have investigated the influence of large tip clearances in turbomachinery components. Large tip clearances are not typically found within axial flow fans and compressors designed for aero-engines. Williams et al. [14] investigated large tip clearances in the high pressure compressor stages used in industrial gas turbines. They have carried out a comprehensive study on two different compressor cascades. They used five-hole pressure probe measurements upstream and downstream of the cascades. The authors have shown that tip leakage flow is a more important parameter influencing the rotor exit flow pattern than blade shape.

Ducted fan VTOL UAVs need to fly in a broad range of atmospheric conditions because of their complicated missions. Their

¹Currently working at Siemens Energy Inc.

²Corresponding author.

Contributed by the International Gas Turbine Institute (IGTI) of ASME for publication in the JOURNAL OF TURBOMACHINERY. Manuscript received November 5, 2012; final manuscript received December 8, 2012; published online September 26, 2013. Editor: David Wisler.

performance is highly affected by large tip clearance. There have been only a few studies about ducted fan aerodynamic and aero-mechanical performance. Pereira performed an experimental study on the effects of various shroud profile shapes on the performance of micro-air vehicle (MAV)-scale shrouded rotors [15]. Seventeen ducted fan models with a nominal rotor diameter of 16 cm (6.3 in.) and various values of diffuser expansion angle, diffuser length, inlet lip radius, and blade tip clearance were tested at various rotor collective angles. Tests performed for an open rotor and a single shrouded-rotor model at a single collective in translational flight, at angles of attack from 0 deg (axial flow) to 90 deg (edgewise flow) and at various advance ratios, are reported.

Martin and Tung [16] tested a ducted fan V/STOL UAV with a 10-inch diameter rotor. They measured aerodynamic loads on the vehicle for different angles of attack (from 0 deg to 110 deg) in hover and different crosswind velocities. Both models were tested with fixed-pitch propellers of varying diameters, in order to test tip clearances from 1% to 4% (based on the rotor tip radius). They also included hot-wire velocity surveys at the inner and outer surfaces of the duct and across the downstream wake, emphasizing the effect of the tip gap on the produced thrust force. In addition, their study showed the effect of the leading edge radius of the duct on the stall performance and stability of the vehicle. They have shown that the thrust of the system decreases with an increasing tip gap height. Their results also showed that for lower rotational speeds, the open rotor thrust was higher than the ducted fan thrust. They explained this by pointing out the increase in viscous losses inside the duct for low rotational speed operations.

Martin and Boxwell [17] tested two ducted fan models that were designed to effectively eliminate the tip leakage. Both models were derived from the baseline (254-mm inner-diameter shroud), which is explained in their previous study [16]. In their first design, they created a notch and fit the propeller inside the

notch. In their second design, a rearward-facing step was cut into the inner shroud. The computational analysis resulted in an increase in the inlet lip suction and an increase in performance. However, the experimental thrust and power measurements showed no difference in the performance of these designs when compared to their baseline duct.

In the present investigation, experimental and computational methods were used to investigate the effect of tip clearance flow on ducted fan aerodynamic performance. A 559 mm ducted fan test system was designed and manufactured for experimental investigations. Total pressure measurements were performed at the downstream of the fan rotor using a traversing Kiel probe. The inlet total pressure and axial velocity were also monitored at the midspan location. The aeromechanical performance of the ducted fan was measured using a six axis force and moment transducer. Besides the experimental measurements, computational analyses were carried out for the ducted fan system in the hover condition. The main goal of this paper is to investigate the large tip clearance effect in ducted fans for VTOL UAV applications. The experimental data obtained were also used to validate the computational method outlined in this paper. The computational method is also going to be used in the development of tip treatments. The results from an investigation dealing with the new tip treatments designed and analyzed using this validated computational approach are presented in an accompanying paper by Akturk and Camci [18].

2 Experimental Method

2.1 Facility Description. The 559 mm diameter ducted fan test system with a realistic disk loading found in most present day VTOL UAV systems is shown in Fig. 1. The main components in the flow path of this facility are listed as follows:

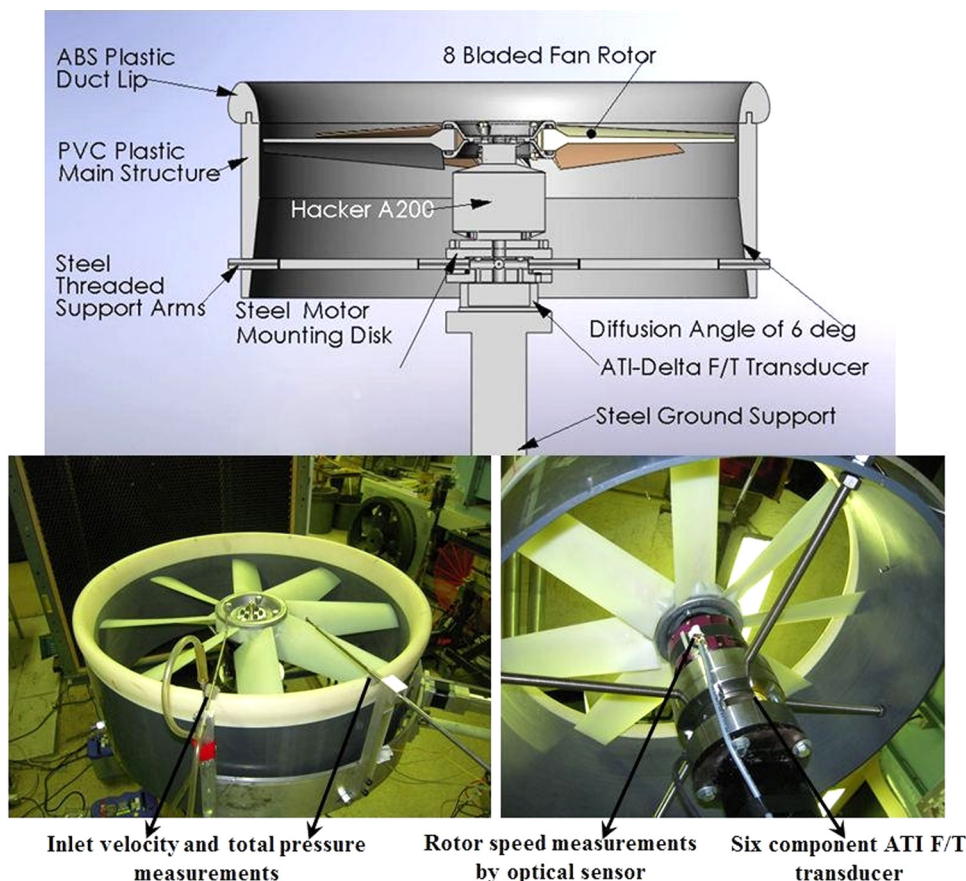


Fig. 1 Schematic and instrumentation of the 559 mm diameter ducted fan system

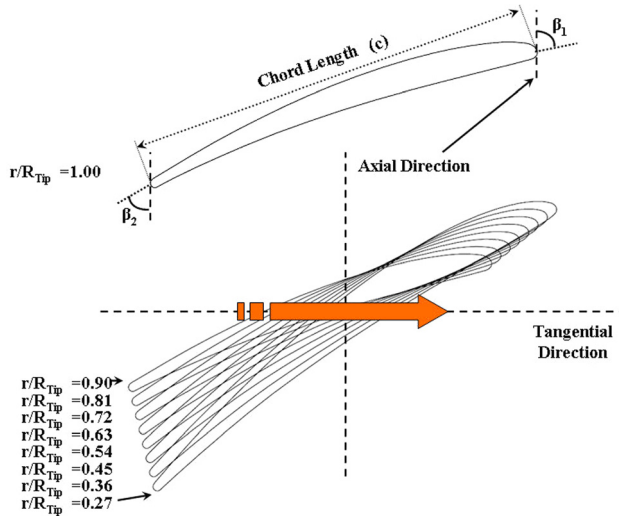


Fig. 2 Blade profiles at various radial stations

- inlet lip section (replaceable)
- eight-bladed axial fan rotor
- 20 hp DC brushless electric motor
- diffuser section
- six component force and torque measurement system

Figure 1 shows the main components of the instrumentation integrated into this research facility. The test system is equipped with a radially traversing Kiel total pressure probe downstream of the axial flow fan rotor, a stationary total pressure probe at the inlet of the duct, an optical once-per-rev sensor, a Pitot probe for velocity measurements at the duct inlet, and an ATI six component force and torque measurement transducer. The system also has a number of thermocouples and various electrical monitoring systems for electrical safety.

2.2 Ducted Fan Model. The ducted fan used in the current experiments is composed of a shroud, axial flow fan, inlet lip, and exit diffuser. The shroud is manufactured from thermoplastic material and has an inner radius of 11.15 in. It is connected to the main support using four 12.7 mm (0.5 in.) diameter stainless steel threaded circular rods. Threaded rods connect the shroud to the central support system. The center support holds the ducted fan so that the fan rotor is about three rotor diameters away from the ground, which guarantees that the measurements are free from the ground effect.

The 559 mm diameter ducted fan was designed to provide a realistic disk loading typical of VTOL UAVs. The 559 mm diameter

ducted fan shown in Fig. 1 provides 828.3 Pa (17.31b/ft²) disk loading under nominal operating conditions (3500 rpm).

The geometry of the duct inlet lip shape can be described by two distinct characteristics: the wall thickness (t_w) and the leading edge radius of curvature (ρ_{LE}). Wall thickness is the maximum thickness of the airfoil shape used to make up the wall of the duct and the leading edge radius of curvature describes the roundness of the duct lip. The inlet lip shape was designed to have a relatively small leading edge radius. The reduced leading edge radius usually allows the adverse pressure gradient to gradually change inside the lip. The changing pressure gradient gradually helps reduce inlet lip separations inside the duct lip, especially under edgewise flight conditions. The t_w and ρ_{LE} used for this ducted fan were 11% and 3.61% of the duct chord, respectively. The diffuser section was designed to augment the thrust generated by the ducted fan. The diffuser half angle at the exit is 6 deg. The axial length of the diffuser is about 117.85 mm (4.64 in.).

2.2.1 Fan Rotor. The eight-bladed fan rotor was designed and manufactured by Multi-Wing International. The fan blades were designed for a high flow coefficient. The rotor blades were manufactured from a high quality thermoplastic (glass reinforced polyamide). The rotor blades are attached to a custom designed aluminum hub. This specific hub system allows for a quick replacement of the rotor assembly in this research facility. Figure 2 shows the blade profiles at various radial stations. Table 1 presents the fan rotor and blade section geometrical properties.

A 20 hp A200-6 brushless electric motor (Hacker) directly drives the axial flow fan rotor in the 559 mm diameter ducted fan research facility. The electric motor was controlled by an electronic speed controller (MasterSPIN-220-OPTO ESC). Electrical power for the motor was supplied by four deep cycle lead acid batteries connected in series. Due to the high torque characteristic of the electric motor, the electric current and temperature of the motor was continuously monitored for operational safety.

2.3 Instrumentation of the 559 mm Ducted Fan

2.3.1 Rotor Exit Total Pressure Measurements. Fan rotor exit total pressure measurements were performed by using a Kiel total pressure probe. The Kiel total pressure probe, having a 5 mm diameter total head, was traversed in the radial direction using a precision linear traverse mechanism. The total pressure probe was always located 45.72 mm downstream of the fan rotor exit plane at 50% blade span (midspan).

The Kiel probe, manufactured by United Sensors Corporation, is relatively insensitive to the incoming angle of the flow (yaw angle). The range of insensitivity to misalignment for this probe is about ± 52 deg to see a more than 1% deviation from the inlet dynamic head [19]. The accurate orientation of the Kiel probe in a

Table 1 Fan rotor geometric and blade section properties

Radius (mm)	r/R_{tip}	Blade section properties		
		β_1	β_2	Chord (mm)
76.2	0.27	71.87	40.77	84.3
101.6	0.36	72.81	43.50	81.5
127.0	0.45	76.56	46.30	78.8
152.4	0.55	78.37	49.94	75.9
177.8	0.64	79.52	52.13	73.1
203.2	0.73	80.31	53.64	70.6
228.6	0.82	82.87	56.51	68.1
254.0	0.91	84.00	58.39	65.8
279.4	1.00	85.21	60.92	63.8

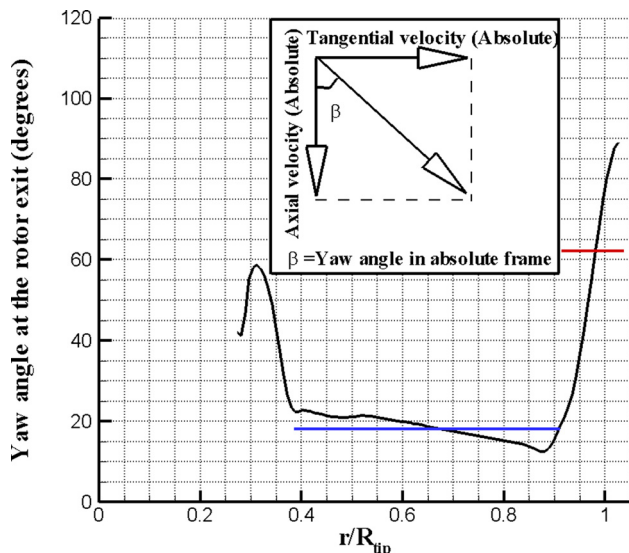


Fig. 3 Yaw angle in the absolute frame calculated from the initial computations

problem where the yaw angle varies dramatically near the tip section of the blade is extremely challenging. A computational fluid dynamics approach was used to properly align the probe with respect to the axial direction. Preliminary computations of the rotor exit flow field were performed using the Ansys CFX RANS solver. Details of this computational analysis can be found in the following sections. Figure 3 shows computed the distribution of the absolute flow yaw angle at the fan rotor exit where the Kiel probe was located. Figure 3 shows that the absolute yaw angle is not significantly changed near the midspan for radial stations $0.38 \leq r/R_{\text{tip}} \leq 0.90$. The average yaw angle obtained on these stations is 18 deg, which is shown by the straight blue line in Fig. 3. The Kiel probe was aligned at this average angle at these locations. Although the flow angles varied by the effect of the three dimensional features such as the passage vortex and hub separation near the hub region, the Kiel probe was assumed to capture the flow field because of its ± 52 deg yaw angle tolerance. Because the tip region where $r/R_{\text{tip}} \geq 0.90$ was affected by the tip leakage vortex, the tangential velocity component changed due to this vortical field and the yaw angle abruptly increased in this region. The Kiel probe was manually aligned by the “averaged” computed absolute flow yaw angles in this region. The probe was aligned at 62 deg angle around the tip region.

The Kiel total pressure head was connected to a Validyne DP 15 variable reluctance pressure transducer that was referenced to atmospheric pressure. The output of the transducer was directly connected to the Validyne CD 15 carrier demodulator that gives a linearized analog output in the range of ± 10 V. The calibration of the pressure transducer required applying a known pressure to the transducer and recording the associated voltage. The relationship between the pressure and voltage was linear because an external demodulator linearization was employed. The Validyne carrier demodulator was connected to a 12-bit data acquisition board (MCC 1208FS). Analog signals were transferred to a computer and analyzed by Labview data acquisition software, which was custom developed for the current research effort. The 5 s data acquisition time was selected as the sampling time for the experiments so that the Kiel probe pneumatic output reached steady state and a statistically stable averaged total pressure reading was recorded.

The inlet conditions for the ducted fan system were also monitored using a Kiel total pressure probe and a conventional Pitot probe. Both probes were mounted over the duct lip at midspan of the fan rotor. The conventional Pitot probe with a static and total hole measured the magnitude of the inlet axial velocity at midspan. The total pressure at the duct inlet was measured using

the same procedure outlined for the rotor exit total pressure probe without “nulling.” The data acquisition time for this probe was also set to 5 s. A Pitot probe was used to obtain the duct inlet velocity. Both probes were aligned with the axial flow direction, since the flow at the inlet of the ducted fan is where the flow was free from tangential and radial components.

2.3.2 Six Component Force and Moment Measurement. The ducted fan aerodynamic research performed in this study requires high accuracy force and moment measurements. The 559 mm diameter fan is equipped with an ATI-Delta six component force and torque transducer. The ATI multi-axis force/torque sensor system measures all six components of the force and moment. Three components of force and three components of moments are measured. It consists of a transducer assembly, a shielded high-flex cable, and a 16-bit data acquisition system and an F/T controller. A software system provided by ATI was used to convert the transducer readings into force and torque output in engineering units using the calibration data provided. The thrust and moment transducer is factory calibrated with known forces and moments. The accuracy of the transducer was ± 0.033 N for forces in the x direction, ± 0.033 N for forces in the y direction, ± 0.099 N for forces in the z direction, ± 0.003 Nm for moments in the x direction, ± 0.003 Nm for moments in the y direction, and ± 0.003 Nm for moments in the z direction.

3 Computational Method

A three dimensional computational method is used for analyzing the viscous and turbulent flow fields around and inside the ducted fan and, especially, the complicated flow field near the fan rotor tip for the hover condition.

A simulation of the incompressible mean flow field around the ducted fan was performed using the general purpose fluid dynamics solver Ansys-CFX. The specific computational system solves the Reynolds-averaged Navier-Stokes (RANS) equations using an element based finite volume method in the ducted fan rotor and around the ducted fan driven VTOL UAV. The mass, momentum, and energy equations are simultaneously solved over an unstructured finite volume based mesh system.

The $k-\omega$ based shear stress transport model is used in our computations [20]. This model accounts for the transport of the turbulent shear stress and gives accurate predictions of the flow separation under an adverse pressure gradient.

3.1 Computational Domains and Boundary Conditions.

The computational analysis for the ducted fan aerodynamic investigation in hover was performed on three separate computational domains that are connected. The stationary inlet and outlet regions and rotating fan rotor region are shown in Fig. 5. The inlet region includes an inlet lip surface that was considered as a solid wall with the no-slip condition. Atmospheric static pressure was prescribed on the top surface. On the side surface, an opening type boundary condition was assumed. An opening boundary condition allows the fluid to cross the boundary surface in either direction. For example, all of the fluid might flow into the domain at the opening, or all of the fluid might flow out of the domain, or a combination of the two might occur. An opening boundary condition might be used where it is known that the fluid flows in both directions (any direction) across the boundary.

The outlet region includes the outer duct surface, circular rods, rotor hub surface, and the support structure underneath the system that is considered as solid walls with the no-slip condition. The bottom surface is also treated with the no-slip boundary condition. On the side surface, an opening boundary condition is assumed.

The rotating region includes fan blades, the rotor hub region, and the shroud surface where rotating fluid motion is simulated by adding source terms. Additional sources of momentum are required to account for the effects of the Coriolis force and the

centrifugal force. Counter-rotating wall velocities are assigned at the shroud surface.

Stationary and rotating regions were subsectional by periodic surfaces. By using the periodicity, the speed of the numerical simulations was increased. The stationary surfaces were divided into four segments and the rotating region was divided into eight periodic segments. Only one of these segments for each region was used in numerical calculations. The difference in the pitch angles of the frames is taken into account in the ninterfaces that are connecting the rotating and stationary surfaces. A stage type interface model was used.

3.2 Stage Interface. When one side is in a stationary frame and the other side is in a rotating frame of reference, an interface should be used for connection. The “stage” type interface model is used in calculations for modeling the frame change. The stage model performs a circumferential averaging of the fluxes on the interface. This model allows steady state predictions to be obtained for turbomachinery components. The stage averaging at the frame change interface introduces a one-time mixing loss. This loss is equivalent to assuming the physical mixing supplied by the relative motion between components. Between the stationary frames, an interface provides a general connection between two stationary domains. The general grid interface is used for mesh connections between interfaces.

3.3 Grid Refinement Study. A grid independence study is performed to show that the computational results are not dependent on the computational mesh and the resolution of the mesh is adequate to capture the significant flow characteristics. The grid independence is evaluated by comparing the computational solutions from three different mesh sizes, comprising a coarse mesh with 3,000,000 tetrahedral cells, a medium mesh with 4,750,000 cells, and a mesh with 6,000,000 cells. The static pressure distribution around the midspan blade profile at the radial station $r = 0.90$ for the baseline fan rotor is plotted in Fig. 4 for three different grid densities. The profile suggests that the computational results are grid independent when the 4,700,000 cells are exceeded. Therefore, the medium mesh is used for all predictions in this chapter. Figure 5 illustrates a view from the medium size computational mesh near the inlet lip region and rotor tip. The unstructured tetrahedral cells are used for the computations. Regions near the solid surfaces are meshed with prisms for generating a better viscous boundary layer grid. A nondimensional wall

distance (y^+) of less than 2 is achieved near the shroud and hub region. The region between the solid shroud and rotating blade tips is filled with prism layers.

4 Experimental Results

4.1 Force and Torque Measurements. The most significant force and moment component that is measured for the ducted fan system in the hover condition is the thrust and rotor torque which are F_z and T_z , as shown in Fig. 1. Other components may become significant when the ducted fan is operated in nonsymmetric inlet conditions, such as forward flight operation. Although three components of forces and moments were measured, only the thrust and torque of the ducted fan will be presented throughout this paper since all of the measurements are performed in the hover condition. The thrust and torque measurements were obtained at the hover condition for a number of rotor speeds. Thrust measurements are normalized as the thrust coefficient, defined as

$$C_T = \frac{\text{Thrust}}{\rho \Omega^2 D^4}, \quad \text{where} \quad \rho = \frac{P_a}{RT_a} \quad (1)$$

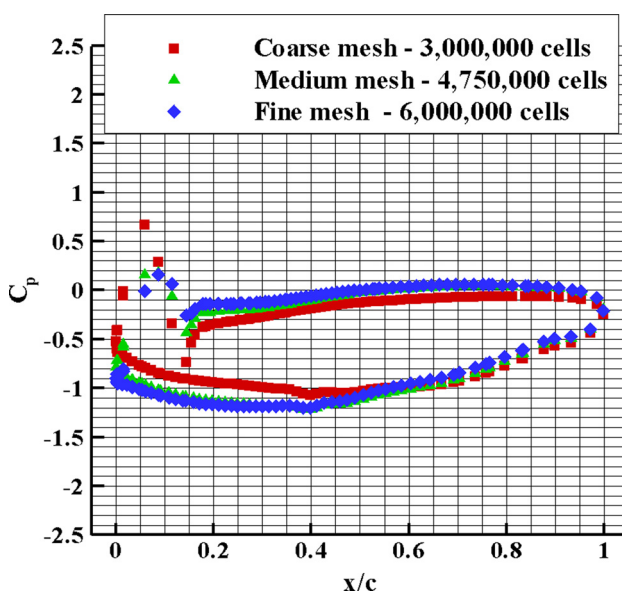
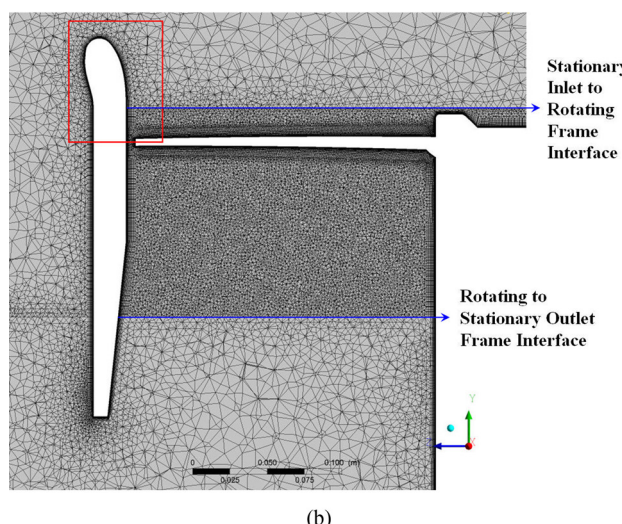
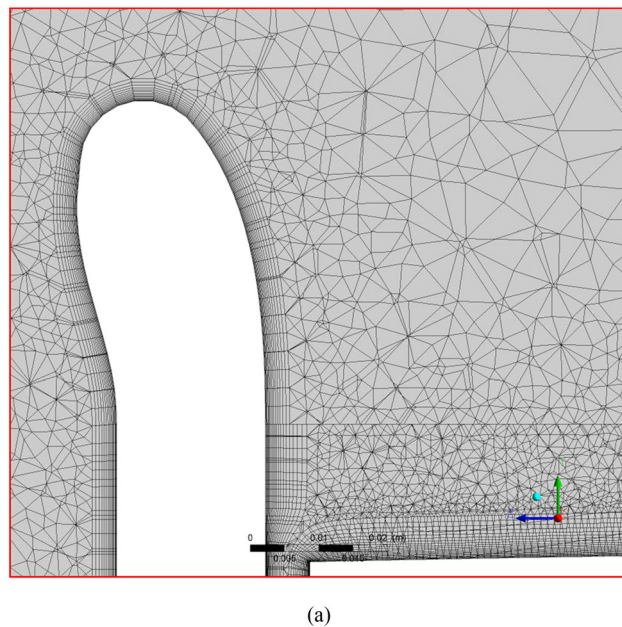


Fig. 4 Grid independence study

Fig. 5 Medium size computational mesh used in the computations

Torque measurements were essential in calculating the required power using the relationship between torque and power (Power = Torque \times Ω). The measured power was normalized as a power coefficient

$$C_P = \frac{\text{Power}}{\rho \Omega^3 D^5}, \quad \text{where} \quad \rho = \frac{P_a}{RT_a} \quad (2)$$

The figure of merit was calculated as a measure of hover efficiency for the ducted fan. The figure of merit was defined as

$$\text{Figure of merit: (FM)} = \frac{C_T^{3/2}}{\sqrt{2} C_P} \quad (3)$$

Figure 6 shows the calculated thrust coefficient for the 559 mm ducted fan with baseline fan rotors at various rotational speeds. The ducted fan thrust was measured for various tip clearances. The fan rotor only thrust was also measured. The fan rotor only thrust was measured by using the 10.89 in. tip diameter fan rotor, which is the identical rotor used for the 3.04% tip clearance study. The tip clearances were adjusted by changing the fan rotor diameter, as previously mentioned.

The variable tip clearance study presented in this chapter used custom made rotors with accurately adjusted tip diameters in a shroud system having a constant inner diameter. Using a ducted fan around an open rotor improves the thrust of the system as compared to an open rotor for tip clearances of 3.04% and 1.71%. For the tip clearance of 5.17%, the open rotor provides more thrust. This observation can be explained by the effect of increased viscous losses and tip leakage related losses. The losses generated when the shroud is added to the fan rotor is so high that the additional thrust due to the duct lip and shroud is almost eliminated. It should also be noted that decreasing the tip gap height is effective at improving the performance of the system and results in an augmented thrust generation.

The thrust force generated per supplied power for various baseline configurations is shown in Fig. 7. The data is arranged in the form of the thrust coefficient C_T versus the power coefficient C_P . The smallest tip clearance configuration generates the highest thrust per unit of power supplied. Since increasing the tip clearance also increases losses in the system, the power demand of the system also increases.

Figure 8 shows another key result of this study. The sensitivity of hover efficiency to increasing tip gap is shown. It should be noted that using a ducted fan configuration also improved hover

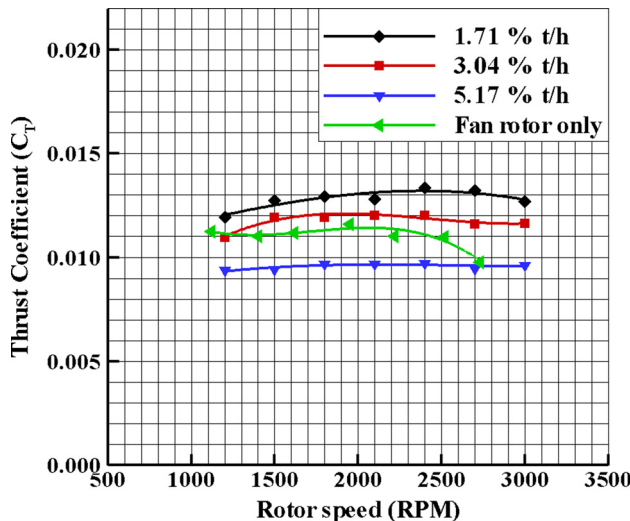


Fig. 6 Thrust coefficient versus the fan rotational speed during hover (baseline rotor)

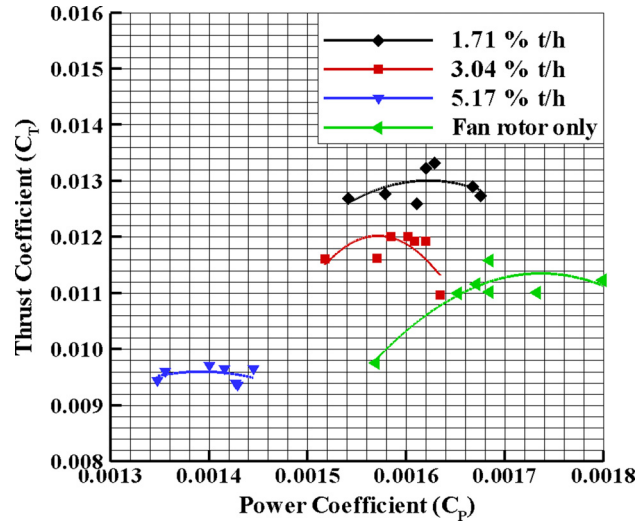


Fig. 7 Thrust coefficient versus the power coefficient for the baseline rotor

efficiency by 38% for the higher rotational speed. Decreasing the tip clearance is effective in increasing the hover efficiency. Decreasing the tip clearance from 3.04% to 1.71% increased the hover efficiency of the system by 17.85% at the higher rotor speed.

4.2 Total Pressure Measurements at Rotor Exit. The aerodynamic performance of the ducted fan was quantified by rotor exit total pressure measurements at the hover condition for 2400 rpm. The results are presented with the nondimensional total pressure coefficient, which is defined as

$$C_{pt} = \frac{P_{te} - P_{ti}}{\frac{1}{2} \rho U_m^2}, \quad \text{where} \quad \rho = \frac{P_a}{RT_a} \quad (4)$$

where U_m is the rotor speed calculated at the midspan $U_m = r_m \times \Omega$. The random uncertainty of the total pressure coefficient was calculated as ± 0.002 [21,22].

Figure 9 shows the total pressure coefficient measured at the downstream position from the rotor hub to the shroud. It should

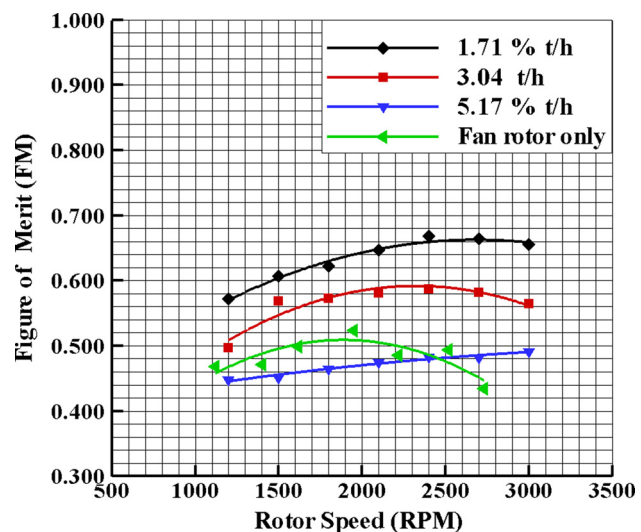


Fig. 8 Figure of merit (FM) versus the fan rotational speed for the baseline rotor

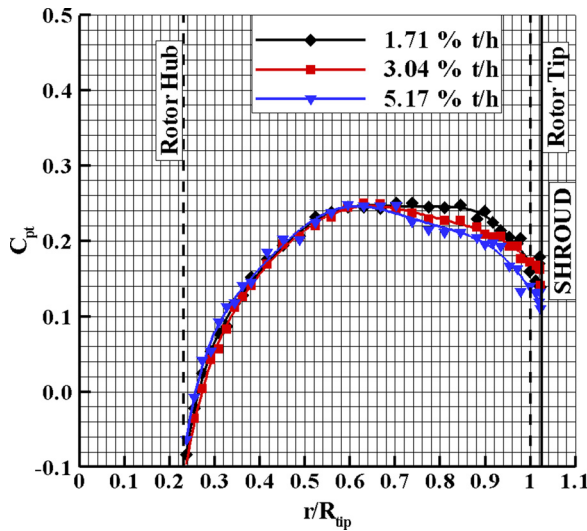


Fig. 9 Total pressure measured downstream of the rotor at 2400 rpm for the baseline rotor

be noted that there is almost no change in the total pressure coefficient by changing the tip clearance for $r/R_{\text{tip}} \leq 0.65$. The flow near the rotor hub is not affected by the tip leakage losses. When the tip clearance is 5.17%, the losses related to the tip leakage vortex are increased at a significant rate because of the increased tip vortex size.

5 Computational Results

5.1 Computational Model Validation

5.1.1 Total Pressure at the Rotor Exit. Figure 10 shows a comparison of the experimental and computational results for 1.71%, 3.04%, and 5.17% tip clearances. The circumferentially averaged total pressure coefficient at the downstream of the fan rotor is compared to the experimental results. The computational and experimental results show very good agreement in the spanwise distribution, except in a limited area near the hub where $r/R_{\text{tip}} \leq 0.65$. The computational results slightly deviate from the experimental results near the hub region. That is because of the highly complex low Reynolds number and, possibly, recirculatory turbulent flow field near the hub region. The low Reynolds number characteristic of the flow makes this computation highly challenging. The Reynolds number based on the blade chord is approximately lower than 50,000 at the $r/R_{\text{tip}} \leq 0.6$. Low Reynolds number flows are relatively hard to compute using standard turbulent models as they are used in present day computational systems. The overall results show significant recirculatory flow zones near the hub wall. The highly 3D and possibly unsteady flow zones are driven by the hub inlet (corner) region flows.

5.1.2 Thrust and Power Curves. Figure 11 shows the variation of thrust with rotational speed obtained from experiments and the computational results for two different tip clearances. Clearly, the computational results agree well with the experimental data for both tip clearances, especially for low rotational speeds. The relative error increases for rotor speeds higher than 2400 rpm.

The computed rotor thrust and duct thrust are also shown in Fig. 11. As the tip clearance increases, the rotor thrust decreases because of the increased tip leakage flow. The tip leakage flow is quantified by calculating the leakage mass flow rate. The leakage mass flow rate is 1.81% of the mass flow rate of the fan rotor for the 1.71% tip clearance. When the tip clearance increased to 3.04%, the leakage mass flow rate is also increased to 3.41% of

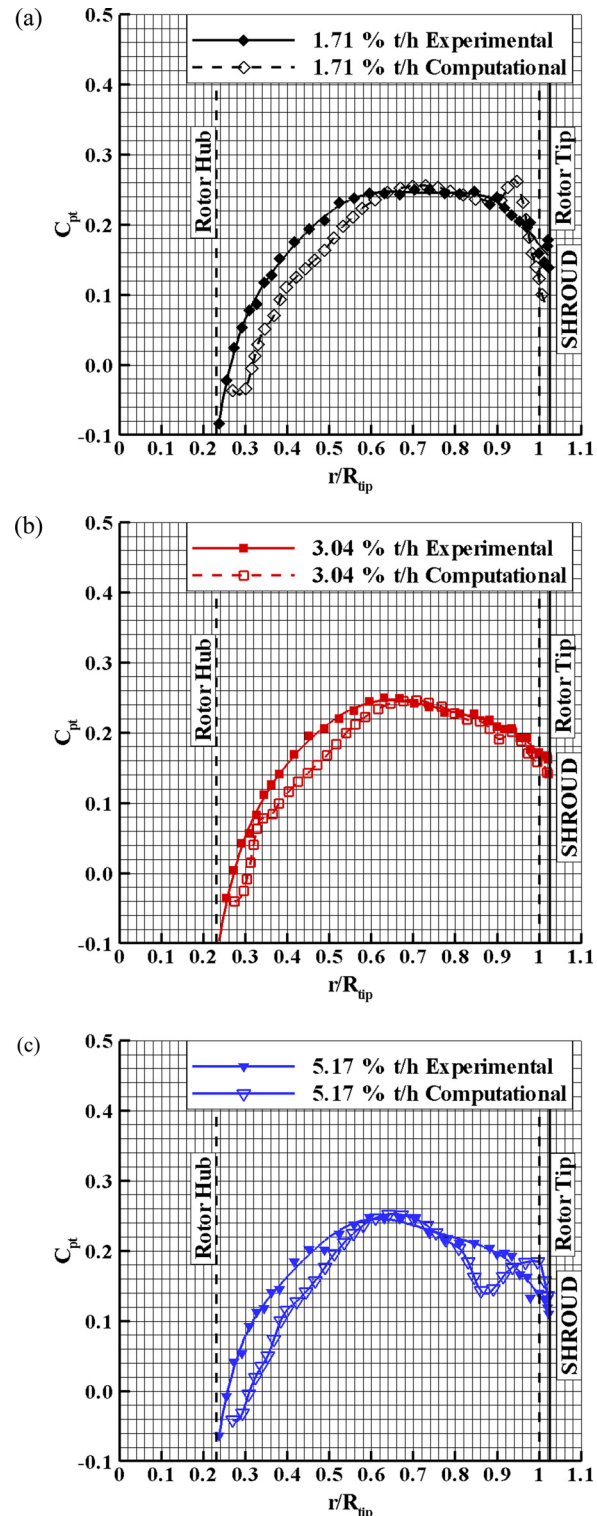


Fig. 10 Total pressure coefficient comparison for experimental and computational analysis at 2400 rpm for the baseline rotor with (a) 1.71%, (b) 3.04%, and (c) 5.17% tip clearances

the fan rotor mass flow rate. That increase in the leakage mass flow rate increased losses in the main fan flow and decreased rotor thrust. Although the duct thrust was the same for both tip clearances for low rotor speeds, it increased for a high rotor speed as the tip clearance decreased. The main reason for this improvement in duct thrust is an increase in the axial velocity component of the velocity, especially for high rotor speeds.

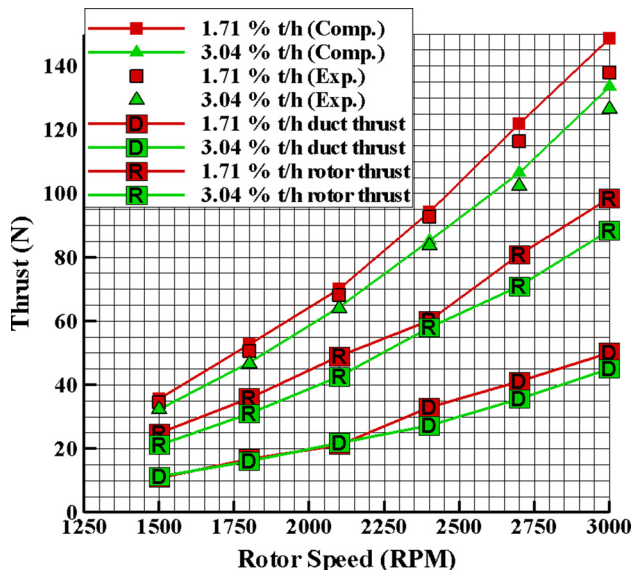


Fig. 11 Comparison of the computed and measured thrust for 1.71% and 3.04% tip clearances for the baseline rotor

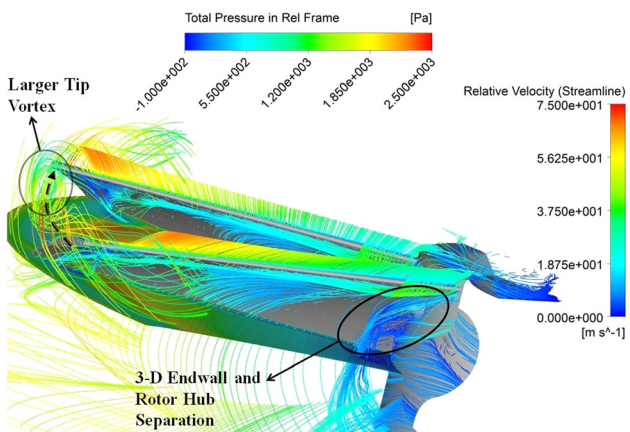


Fig. 12 Streamlines around the baseline rotor blade with a 1.71% tip clearance and the rotor hub at 2400 rpm

5.2 Flow Field Analysis

5.2.1 Effect of Tip Leakage and Secondary Flows on Fan Rotor Exit Performance. The flow field between the stationary shroud and rotor tip of a ducted fan is highly complex because of the interaction of the leakage flow, annulus wall boundary layer, and rotor wake. Figures 12 and 14 show the streamlines drawn around the rotor blade with the 1.71% and 3.04% tip clearance, respectively. The complex flow features near the tip and midspan region are visualized at a high spatial resolution. Streamlines are colored by the relative velocity magnitude and drawn in the relative frame of reference. The leakage vortex impinges on the neighboring blade and creates a local loss region. This lossy region moves towards the midspan as the clearance increased. The magnitude of the relative total pressure just at the downstream of the fan rotor with 1.71% tip clearance is shown in Fig. 13. This figure is drawn just downstream of the fan rotor and the visualization plane is aligned with the trailing edge of the rotor blade. The red regions in the figure show the highest total pressure regions, while dark blue region show the lowest total pressure regions. The dark blue region near the fan rotor hub clearly shows the loss generation near the endwall surface due to the combination of the hub-corner separation and the three dimensional hub endwall flow.

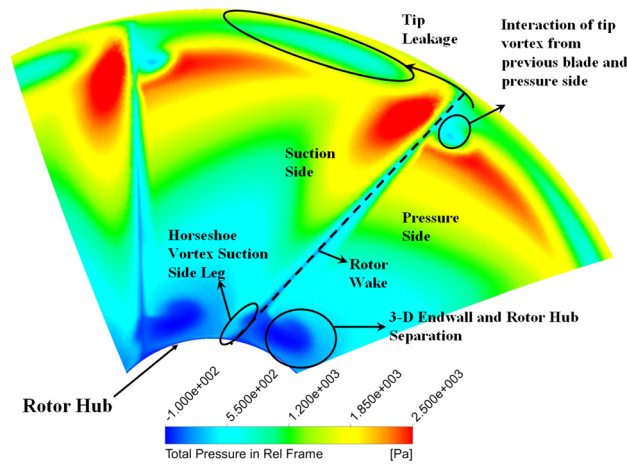


Fig. 13 Relative total pressure distribution at the rotor exit plane for the baseline blade with a 1.71% tip clearance

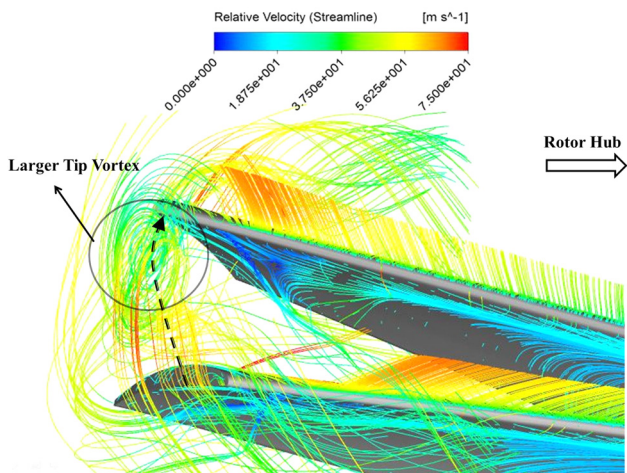


Fig. 14 Streamlines around the baseline rotor blade with a 3.04% tip clearance and the rotor hub at 2400 rpm

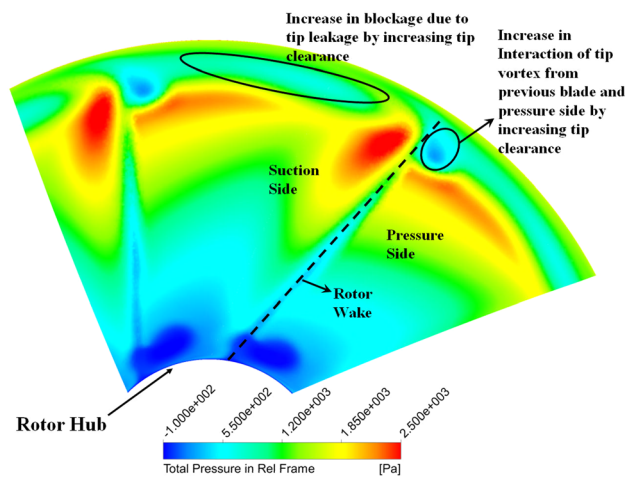


Fig. 15 Relative total pressure distribution at the rotor exit plane for the baseline blade with a 3.04% tip clearance

The wake region of the rotor blade is shown by dashed lines in Fig. 13. The tip leakage flow and tip vortex is also visible near the rotor tip. The light blue region near the rotor tip shows the blockage effect that is induced by the tip vortex originating from the

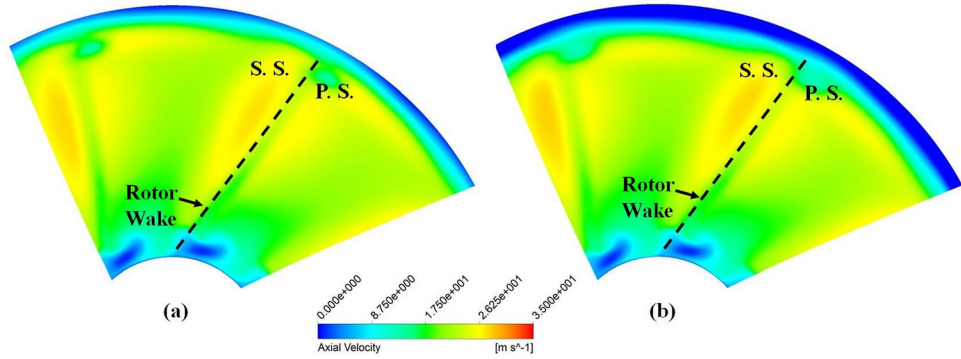


Fig. 16 Axial velocity comparison at the rotor exit plane for the baseline blade with (a) 1.71%, and (b) 3.04% tip clearances

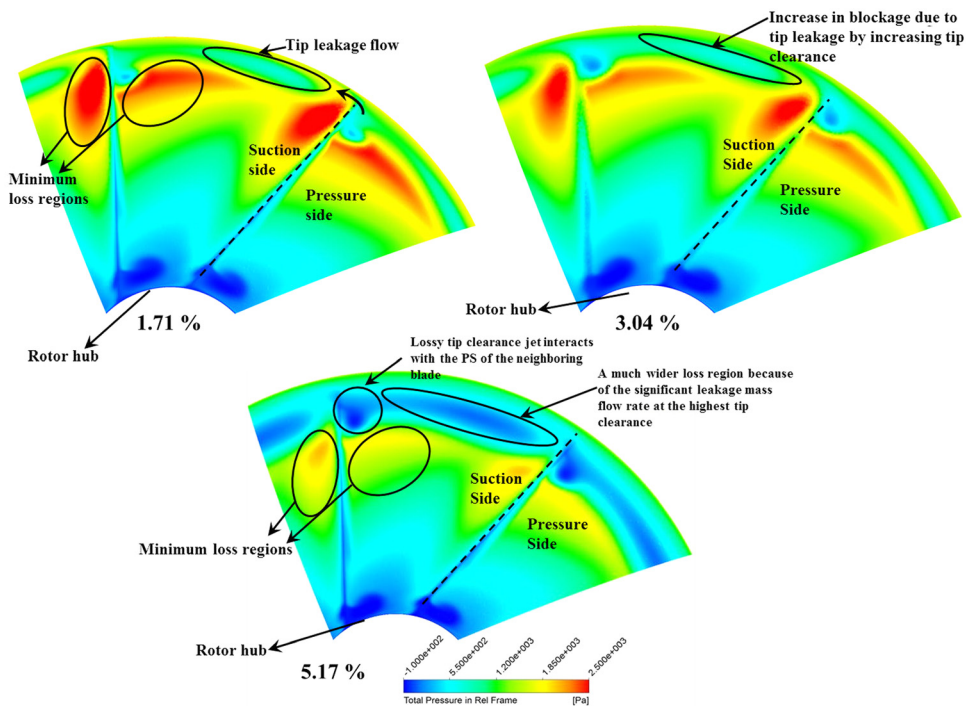


Fig. 17 Relative total pressure comparison at the rotor exit plane for the baseline blades with 1.71%, 3.04%, and 5.17% tip clearances

rotor blade pressure side. There is also another light blue region near the pressure side of the rotor blade. That shows the interaction of the tip vortex propagating from the previous rotor blade with the pressure side, as shown in Fig. 13. This interaction can also be seen in Fig. 12 by the streamlines drawn around the rotor tip. This interaction near the pressure side results in a measurable total pressure drop at the exit of the fan blade because of separation from the pressure side.

Figure 15 shows the effect of the tip clearance and other important 3D passage flow features on the rotor exit relative total pressure distribution for a tip clearance value of 3.04%. This figure is drawn at the same plane that is used in Fig. 13. Changing the clearance level did not affect this distribution near the hub region. However, an increase in the tip clearance resulted in more aerodynamic loss near the rotor tip. The overall blockage due to tip leakage is also increased. Besides, the interaction of the tip vortex and rotor blade pressure side is greatly enhanced and more total pressure loss is obviously generated in the passage. Figure 16 shows the comparison of the axial velocity at the downstream of the fan rotor. The low momentum fluid near the hub region is

shown by a dark blue color. This region was not affected by changing the tip clearance level. The tip leakage losses were increased by increasing the tip clearance. An increase in the size of the blockage due to the tip vortex is observed by comparing the dark blue regions near the casing for 1.71% and 3.04% tip clearances. The size of the dark blue area increased for the 3.04% tip clearance.

The effect of increasing the tip clearance is shown in Fig. 17. Three different tip clearances were compared by total pressure contours drawn at the downstream of the fan rotor and the visualization plane is aligned with the trailing edge of the rotor blade. When the tip clearance was increased to 5.17%, tip leakage losses were tremendously increased due to a stronger tip clearance jet. This lossy leakage flow interacts with the pressure side of the neighboring blade. This impinging leakage jet creates a relatively large local loss region and moves towards the mid span. A much wider total pressure loss region was created because of the significant leakage mass flow rate at the highest tip clearance. The minimum loss regions indicated by red are shrinking, as shown by the orange and yellow zones for the 5.17%.

6 Conclusions

Experimental investigations and computational analyses were performed for the development of novel tip geometries that are applicable to ducted fans used in VTOL UAV systems. The computational method that will be a major design analysis tool for the design of novel tip geometries is validated via experimental data presented throughout this paper.

A 559 mm diameter ducted fan test system was designed and manufactured for experimental investigations of tip leakage flow in ducted fans. Fan rotor exit total pressure surveys and duct inlet total pressure and velocity measurements were carried out for aerodynamic performance quantifications. A six component force and torque transducer was used for aeromechanical performance quantification.

A high resolution simulation of the flow field around the rotating fan rotor blades was performed by solving Reynolds-averaged Navier-Stokes equations using a general purpose solver, Ansys-CFX. The computational analysis was extensively used in designing the tip treatments.

When the 3.04% clearance results are compared to the rotor only result, up to a 38% increase in ducted fan hover efficiency can be obtained at higher rotor speeds. That increase is mainly the result of using a duct around an open rotor.

A steady-state RANS simulation of fan rotor blades and duct geometry showed very good agreement with the measured total pressure distribution, especially near the tip region of the rotor in the 559 mm diameter ducted fan research facility.

Experimental investigations of the baseline rotor showed that decreasing the tip clearance increased the thrust obtained from the ducted fan in the hover condition. Decreasing the tip clearance from 3.04% to 1.71% also increased the hover efficiency of the system by 17.85% at higher rotor speeds.

When the tip clearance increased from 3.04% to 5.17%, up to an 18.1% drop in hover efficiency was observed.

Since the agreement between the experimental results obtained from the 559 mm diameter ducted fan and the 3D RANS based computations is very good, the present computational tool forms a strong design/analysis basis for future tip treatments that can be developed by computational means.

The results from an investigation dealing with the new tip treatments designed and analyzed using this validated computational approach are presented in an accompanying paper by Akturk and Camci [18].

Acknowledgment

The authors acknowledge the financial support provided by the PSU Vertical Lift Center of Excellence (VLRCOE) and the National Rotorcraft Technology Center (NRTC) (Under U.S. Army Research Office Grant No. W911W6-06-2-0008). They wish to thank Ozhan Turgut for his support throughout this effort. They are also indebted to Mr. Harry Houtz for his technical support.

Nomenclature

c = chord length

C_p = static pressure coefficient

C_{pt} = total pressure coefficient, $C_{pt} = P_{te} - P_{ti}/(1/2)\rho U_m^2$

C_P = power coefficient, $C_P = \text{Power}/\rho\omega^3 D^5$

C_T = thrust coefficient, $C_T = \text{Thrust}/\rho\omega^2 D^4$

D = shroud (casing) inner diameter (m)

h = blade height

IC = internal combustion

p = static pressure

PS = pressure side

R = ideal gas constant (for air $R = 287 \text{ J/Kg K}$)

RANS = Reynolds-averaged Navier-Stokes

SS = suction side

t = effective tip clearance in inches

t/h = relative tip clearance with respect to blade height

UAV = uninhabited aerial vehicles

VTOL = vertical take-off and landing

y^+ = nondimensional wall distance

References

- [1] Lee, G. H., Baek, J. H., and Myung, H. J., 2003, "Structure of Tip Leakage in a Forward Swept Axial-Flow Fan," *Flow, Turbul. Combust.*, **70**, pp. 241–265.
- [2] Jang, C. M., Furukawa, M., and Inoue, M., 2001, "Analysis of Vortical Flow Field in a Propeller Fan by LDV Measurements and LES—Part I: Three-Dimensional Vortical Flow Structures," *ASME J. Fluids Eng.*, **123**(4), pp. 748–754.
- [3] Jang, C. M., Furukawa, M., and Inoue, M., 2001, "Analysis of Vortical Flow Field in a Propeller Fan by LDV Measurements and LES—Part II: Unsteady Nature of Vortical Flow Structures Due to Tip Vortex Breakdown," *ASME J. Fluids Eng.*, **123**(4), pp. 755–761.
- [4] Storer, J. A. and Cumpsty, N. A., 1991, "Tip Leakage Flow in Axial Compressors," *ASME J. Turbomach.*, **113**(2), pp. 252–259.
- [5] Lakshminarayana, B., Zaccaria, M., and Marathe, B., 1995, "The Structure of Tip Clearance Flow in Axial Flow Compressors," *ASME J. Turbomach.*, **117**, pp. 336–347.
- [6] Matzgeller, R., and Burgold, Y., 2010, "Investigation of Compressor Tip Clearance Flow Structure," *Proceedings of the ASME Turbo Expo 2010: Power for Land, Sea and Air*, Glasgow, UK, June 14–18, *ASME* Paper No. GT2010-23244.
- [7] Inoue, M., Kuroumaru, M., and Furukawa, M., 1986, "Behavior of Tip Leakage Flow Behind an Axial Compressor Rotor," *ASME J. Gas Turbines Power*, **108**, pp. 7–14.
- [8] Furukawa, M., Inoue, M., Kuroumaru, M., Saik, I. K., and Yamada, K., 1999, "The Role of Tip Leakage Vortex Breakdown in Compressor Rotor Aerodynamics," *ASME J. Turbomach.*, **121**, pp. 469–480.
- [9] Fujita, H. and Takata, H., 1984, "A Study on Configurations of Casing Treatment for Axial Flow Compressors," *Bull. JSME*, **27**, pp. 1675–1681.
- [10] Moore, R. D., Kovich, G., and Blade, R. J., 1971, "Effect of Casing Treatment on Overall and Blade-Element Performance of a Compressor Rotor," NASA Technical Report No. TN-D6538.
- [11] Reynolds, B., Lakshminarayana, B., and Ravindranath, A., 1979, "Characteristics of Near Wake of a Fan Rotor Blade," *AIAA J.*, **17**, pp. 959–967.
- [12] Ravindranath, A. and Lakshminarayana, B., 1980, "Mean Velocity and Decay Characteristics of Near and Far-Wake of a Compressor Rotor Blade of Moderate Loading," *ASME J. Eng. Power*, **102**, pp. 535–547.
- [13] Myung, H. J. and Baek, J. H., 1999, "Mean Velocity Characteristics Behind a Forward Swept Axial-Flow Fan," *JSME Int. J.*, **42**, pp. 476–488.
- [14] Williams, R., Ingram, G., and Gregory-Smith, D., 2010, "Large Tip Clearance Flows in Two Compressor Cascades," *Proceedings of the ASME Turbo Expo 2010: Power for Land, Sea and Air*, Glasgow, UK, June 14–18, *ASME* Paper No. GT2010-22952.
- [15] Pereira, J. L., 2008, "Hover and Wind-Tunnel Testing of Shrouded Rotors for Improved Micro Air Vehicle Design," Ph.D. thesis, University of Maryland, College Park, MD.
- [16] Martin, P. and Tung, C., 2004, "Performance and Flowfield Measurements on a 10-Inch Ducted Rotor VTOL UAV," *60th Annual Forum of the American Helicopter Society*, Baltimore, MD, June 7–10.
- [17] Martin, P. B., and Boxwell, D. A., 2005, "Design, Analysis and Experiments on a 10-Inch Ducted Rotor VTOL UAV," *AHS International Specialists Meeting on Unmanned Rotorcraft: Design, Control and Testing*, Chandler, AZ, January 18–20.
- [18] Akturk, A., and Camci, C., 2011, "Tip Clearance Investigation of a Ducted Fan Used in VTOL UAVS—Part II: Novel Treatments Via Computational Design and Their Experimental Verification," *Proceedings of the ASME Turbo Expo 2011: Power for Land, Sea and Air*, Vancouver, Canada, June 6–10, *ASME* Paper No. GT2011-46359.
- [19] United Sensors Corp., 2011, "Kiel Probes: General Information," <http://www.unitedsensorcorp.com/kiel.html>
- [20] Wilcox, D. C., 1993, *Turbulence Modeling for CFD*, DCW Industries, La Cañada, CA.
- [21] Abemethy, R. B., Benedict, R. P., and Dowdell, R. B., 1985, "ASME Measurement Uncertainty," *ASME J. Fluids Eng.*, **107**(2), pp. 161–163.
- [22] Abemethy, R. B., and Ringhiser, B., 1985, "The History and Statistical Development of the New ASME-SAE-AIAA-ISO Measurement Uncertainty Methodology," *AIAA/SAE/ASME/ASEE 21st Joint Propulsion Conference and Exhibit*, Monterey, CA, June 8–10.